





Cs_xWO₃@NBs as a Multi-Image Guided Photothermal/Photodynamic Combination Therapy Platform for the Treatment of Hepatocellular Carcinoma

Chunyue Wang , Xiaodong Wang , Yuhang Tian, Huimin Tian , Yichi Chen, Bolin Wu, Wen Cheng 

Department of Ultrasound, Harbin Medical University Cancer Hospital, Harbin, People's Republic of China

Correspondence: Wen Cheng, Department of Ultrasound, Harbin Medical University Cancer Hospital, No. 150, Haping Road, Nangang District, Harbin, 150081, People's Republic of China, Tel +86 13313677182, Fax +86 451 85718392, Email chengwen@hrbmu.edu.cn

Purpose: Effective cancer treatment relies on the precise deployment of clinical imaging techniques to accurately treat tumors. One highly representative technology among these is multi-imaging guided phototherapy. This work introduces a new and innovative theranostic drug that combines near-infrared (NIR) irradiation-induced photodynamic therapy (PDT) and photothermal therapy (PTT) to treat malignancies. Moreover, it can be utilized as a contrasting substance for X-ray computed tomography (CT) imaging and contrast-enhanced ultrasound (CEUS) to aid in the administration of therapy.

Methods: Cesium tungsten bronze nanobubbles (Cs_xWO₃@NBs) were constructed via a water-controlled solvothermal synthesis and thin film hydration of phospholipid. Various methods, including dynamic light scattering, transmission electron microscopy, and X-ray photoelectron spectroscopy, were used to analyze and describe the size, shape, and chemical characteristics of the nanoparticles. In this study, hepatoma cell lines HepG2 and HUH7 were employed in vitro, and xenotransplantation mouse models were used to assess their antitumor effects. A series of in vitro and in vivo trials were conducted to assess the effectiveness of combining photodynamic and photothermal therapies, as well as using CEUS and CT imaging.

Results: The Cs_xWO₃@NBs exhibit photothermal effects and the generation of reactive oxygen species (ROS) under laser irradiation, thereby enabling effective photothermal and photodynamic combinatorial therapy. Following combined treatment, the activity and invasive capacity of hepatocellular carcinoma cells were markedly diminished, the development rate of the tumor was noticeably reduced, and the level of biological toxicity was low. Additionally, Cs_xWO₃@NBs possess the capacity to serve as both a CT imaging agent and a contrast-enhanced ultrasound agent.

Conclusion: Cs_xWO₃@NBs represent a promising theranostic agent for image-guided cancer therapy.

Keywords: photodynamic therapy, photothermal therapy, imaging, apoptosis, hepatocellular carcinoma

Introduction

Further research into cancer treatments is vital if we are to improve outcomes for all patients affected by this disease. Notwithstanding the considerable advances made in the treatment of numerous cancer types in recent decades, efficacious therapies for certain forms of cancer, such as liver cancer, remain elusive. It is estimated that tens of thousands of people die of cancer each year.^{1,2} Furthermore, numerous patients who have undergone successful treatment with traditional therapies subsequently experience the long-term adverse effects of these therapies, including an increased risk of developing a second cancer.³⁻⁵ It thus falls upon us as a scientific community to develop cancer treatments that either prevent or reduce the occurrence of side effects, thereby ensuring that every cancer patient can receive safe and effective treatment with the highest possible quality of life. Among the treatments currently in development, those based on light activation, such as photodynamic therapy (PDT) and photothermal therapy (PTT), represent a new avenue for

improving the time and quality of cancer patients' lives.^{6–9} Extensive studies have been conducted on the potential use of PDT and PTT in fundamental cancer therapy research and preclinical testing, owing to their numerous benefits. These include reduced invasiveness, fewer side effects and damage to surrounding tissues, and the potential to overcome drug resistance.^{10–14} The combination of PDT and PTT represents a promising strategy for enhancing the efficacy of cancer treatment.^{15–19} Consequently, it is of greater importance to develop a photosensitizer that combines PDT and PTT under the excitation of laser for tumor phototherapy.

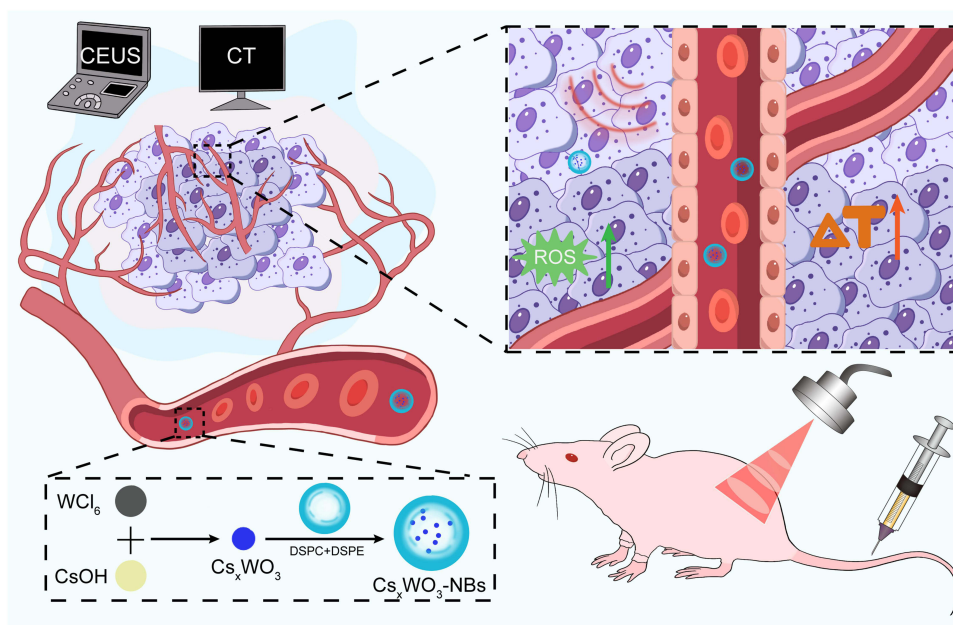
PDT and PTT are two distinct phototherapy methods that utilize specific therapeutic agents to destroy cells under the influence of appropriate light irradiation. PDT consists of three essential elements: a photosensitizer, a laser, and oxygen.^{16,20} When the photosensitizer is exposed to the laser, it undergoes irradiation, which triggers a photochemical reaction leading to the creation of a very reactive substance called ROS (reactive oxygen species). The latter can rapidly cause significant toxicity, which may result in cell death through apoptosis or necrosis.^{21,22} In addition to direct cytotoxic effects, PDT can also damage tumor vessels and induce a strong inflammatory response to combat tumors.^{23,24} In contrast to PDT, the mechanism of PTT is to induce a rapid local increase in temperature at the treatment site. In this process, photothermal agents (PTAs) induce temperature elevations through the non-radiative relaxation of excited electrons.^{25–27} PTT has been demonstrated to induce direct tumor cell death.²⁸ The application of hyperthermia to tumors results in the denaturation of a proportion of thermolabile cellular proteins, which subsequently co-aggregate with native, aggregative-sensitive proteins.^{29,30} Hyperthermia causes denaturation and aggregation of proteins, which has significant effects on subsequent processes such as protein inactivation, chromatin modification, and suppression of DNA synthesis and repair. Eventually, these effects lead to the destruction of tumor cells.^{30–34}

In a controlled on-demand drug delivery system, the key factors are the timing, location, and method of triggering the release of the drug.^{35,36} The nano-bubble coated with gas represents a category of ultrasonic responsive material.^{37,38} Nanovesicles function as a contrast agent, markedly augmenting tumor echogenicity and facilitating the guidance of therapy. This is achieved by enabling the identification of tumor lesions and the determination of the drug's arrival time.^{37,39–42} In contrast, nanobubbles display a propensity for instability.⁴³ The sustained ultrasound radiation would induce the drug-laden vesicles to explode instantaneously, which would remotely activate a smart gate “switch” at a pre-designed point in time and result in the rapid release of the drug.^{44–46} This study aims to introduce a new medicinal substance, cesium-tungsten bronze (Cs_xWO_3), which is created by incorporating Cs ions into the WO_3 structure to produce an N-type metal. The resulting Cs_xWO_3 is a material that can capture NIR and has a wide absorption spectrum in the NIR range (780–2500 nm). It shows both PTT and PDT effects. To achieve a satisfactory photothermal and photodynamic treatment effect, cesium-tungsten bronze (Cs_xWO_3) nanorods were selected as the sensitizer of NIR. The natural abundance of the W element in Cs_xWO_3 is higher than that of the Au element, which results in a high photothermal conversion efficiency, thereby offering a promising prospect for PTA application.^{47,48} Furthermore, the element W of Cs_xWO_3 possesses a relatively high atomic number ($Z=74$) and a notable X-ray attenuation coefficient, rendering it a suitable contrast enhancement agent in CT imaging.^{49–51} As is shown in Scheme 1, we first synthesized Cs_xWO_3 , and then used a phospholipid membrane to wrap Cs_xWO_3 and C_3F_8 to form phospholipid nanobubbles Cs_xWO_3 @NBs, to obtain nanoparticles with quadruple functions (PDT, PTT, CT and CEUS).

Materials and Methods

Synthesis of Cs_xWO_3

Initially, 0.2976 g of WCl_6 was completely dissolved in 40 mL of anhydrous ethanol with intense stirring. Subsequently, 0.063 g of $\text{CsOH}\cdot\text{H}_2\text{O}$ was introduced to the resulting yellowish ethanol solution of WCl_6 . After achieving homogeneity, 10 mL of acetic acid was introduced to the mixture. The mixture obtained was thereafter moved to a Teflon-lined autoclave with a capacity of 100 mL. Solvothermal reactions were then carried out in an electric oven at a temperature of 200 °C for a duration of 20 hours. Following the process, the resulting dark blue substances were subjected to centrifugation, washed four times with water and ethanol, and subsequently dried under vacuum conditions at a temperature of 60 °C. Lastly, they were ground into blue powder.



Scheme 1 Schematic illustration of Cs_xWO_3 @NBs mediated antitumor.

Synthesis of Cs_xWO_3 @NBs

The NBs were produced using a modified emulsification technique. Three types of liposomes, namely DSPC, DSPE-PEG2000, and DSPE-PEG2000-biotin, were obtained from Avanti Polar Lipids (Alabaster, AL, USA). These liposomes were mixed in a molar ratio of 9:1:1. A certain quantity of phospholipids was dissolved in a solvent mixture of chloroform and methanol (in a ratio of 2:1, volume to volume). Subsequently, the mixture was transferred to a rotary vacuum evaporator to eliminate the solvent at a temperature of 45°C. The process of dissolving and evaporating was repeated three times. The desiccated phospholipid compounds were rehydrated in 5 mL of phosphate-buffered saline (pH 7.4) at ambient temperature. Subsequently, the Cs_xWO_3 powder was introduced into the liposomal suspension. Afterward, the suspension was transferred into a small sample vial, and the air above the solution was removed and replaced with C_3F_8 gas. The solution was additionally stirred for 45 seconds using a dental amalgamator (YJT Medical Apparatuses and Instruments, Shanghai, China), and thereafter placed in 5 mL of sterile PBS. The liquid portion was collected to obtain the Cs_xWO_3 @NBs.

Characterization

The crystal properties of Cs_xWO_3 were analyzed using the Shimadzu XD-D1 instrument. The optical properties of the materials were measured by the U-4100 spectrophotometer of Hitachi. Zeta potential tests were performed on a zeta potential analyzer (zeta PALS BI-90 Plus, Brookhaven Instruments). The shape of Cs_xWO_3 @NBs was examined using the transmission electron microscope (TEM, Hitachi TEM system, Japan). The particle size and zeta potential were measured by dynamic light scattering (DLS, Nano-2s ZEN3600, Malvern Panalytical Limited, UK).

Photothermal Test

A 0.45 mL solution of Cs_xWO_3 in water was placed in a quartz tube having a volume of 0.5 mL. The dispersion was thereafter exposed to irradiation using a NIR laser at a power density of 2.0 W/cm^2 for a duration of 10 minutes. An infrared camera (FLIR System i7) was used to monitor the temperature during the process.

Detection of Reactive Oxygen Species (ROS)

ROS was detected in 1,3-diphenylisobenzofuran (DPBF) probe solution or DPBF solution supplemented with Cs_xWO_3 @NBs (0.125 mg/mL). After laser irradiation (2 W/cm^2) for 1, 3, 5, 7, and 10 min, the ROS formation was

determined, and the absorbance at 420 nm was determined with a spectrophotometer (U-4100, Hitachi). As a control, the absorption spectra of water were also examined under the same conditions. Intracellular ROS detection was performed by staining HepG2 and HUH7 cells with 2,7-dichlorodihydrofluorescein diacetate (DCFH-DA, Beyotime, Jiangsu, China). Including the untreated control group, NIR irradiation group, Cs_xWO₃@NBs incubation group, Cs_xWO₃@NBs mediated phototherapy group, and Cs_xWO₃@NBs mediated phototherapy plus VC group. The cells underwent different treatments with DCFH-DA for a duration of 20 minutes at 37°C. Following that, the cells were examined utilizing a fluorescent microscope (LX71, Olympus, Tokyo, Japan) to determine the findings.

In vitro CEUS and CT Imaging

The diagnostic capabilities of Cs_xWO₃@NBs as an ultrasonic contrast agent were investigated in a rubber tube that simulated blood arteries. The Cs_xWO₃@NBs suspension (2.0 mg/mL 100 μL) was injected into a latex tube and imaging was done utilizing Resona R9 (Mindray, China) in B-mode and contrast mode with phosphate-buffered saline (PBS) as a control ultrasound. For CT imaging detection, a series of Cs_xWO₃@NBs solutions with the same concentration (1.25, 2.5, 5, 10, and 20 mg/mL, respectively) were put in clear Eppendorf tubes with PBS as the blank group. The Eppendorf tubes were assembled and fastened to the stent. Images were captured with a CT scanner (PE quantum gxII, Laboratory for Space Environment and Physical Sciences, Harbin Institute of Technology, Harbin, China).

In vivo CEUS and CT Imaging

To test the capacity of the Cs_xWO₃@NBs to CEUS in vivo, a subcutaneous mouse model of the HepG2 tumor was developed. Female Balb/c thymus-free mice were procured from Liaoning Life Changsheng Biotechnology Co., LTD. (Liaoning Province, China) for in vivo testing. They were housed in a pathogen-free environment with a 12-hour light/dark cycle and acclimated to the surroundings over three days. HepG2 cells (3 × 10⁶ cells/only) were administered subcutaneously. When the tumor volume reached 180–200 mm³, mice received an intratumoral injection of Cs_xWO₃@NBs. Resona R9 (Mindray, China) was then utilized to collect B-mode US and CEUS pictures of tumor-bearing mice before and following injection, as well as echo signal strength in the region of interest. CT Images were captured with a CT scanner (PE quantum gxII, Laboratory for Space Environment and Physical Sciences, Harbin Institute of Technology, Harbin, China). Finally, imaging analysis software ImageJ (National Institutes of Health, Bethesda, MD, USA) and SimpleViewer were used to determine the intensity of the specific area being examined.

In vivo Fluorescence Imaging

Fluorescent agent of choice was fat-soluble 1, 1'-Dioctadecyl-3 filling', 3'-Tetramethylindotricarbocyanine Iodide (DIR). DIR was added to the phospholipid dissolving process of Cs_xWO₃@NBs synthesis to obtain fluorescence DIR labeled Cs_xWO₃@NBs (DIR-Cs_xWO₃@NBs). The mice tumor models used for in vivo fluorescence imaging were consistent with those used in vivo US and CT imaging experiments. When the tumor volume reached 180–200 mm³, mice received an intratumoral injection of DIR-Cs_xWO₃@NBs (0.5 mg/mL 100 μL). Fluorescence images were captured with a fluorescence imaging scanner (PE quantum gxII, Laboratory for Space Environment and Physical Sciences, Harbin Institute of Technology, Harbin, China). LivingImage software was used to determine the fluorescence intensity of the specific area being examined.

Cell Culture

This experiment involved the inclusion of the human liver cancer cell lines HepG2 and HUH7. The cells were acquired from the Cell Bank of the Chinese Academy of Sciences (Shanghai, China). The cells were grown in DMEM media supplemented with 10% FBS in a humidified incubator maintained at 37°C and 5% CO₂. The overall cell count was measured using a hemocytometer (Bürker-Türk). Cells that were developing at an exponential rate were employed for all studies.

Cell Toxicity Assay

The toxicity of $Cs_xWO_3@NBs$ was assessed using the Cell Counting Kit-8 (CCK-8) assay. HepG2 and HUH7 cells in the logarithmic growth phase were initially placed in 96-well assay plates at a density of 3×10^3 cells per well. After 24 hours, the cells were exposed to different doses of $Cs_xWO_3@NBs$ or subjected to various treatment groups for an additional 24 hours. Following three washes with a PBS solution, 10 μ L of CCK-8 solution was introduced to each well and left for a duration of 2 hours. The cellular toxicity was assessed using a microplate reader (BioTek, Winooski, VT, USA) by measuring the absorbance at 450 nm.

Cell Apoptosis Assay

The Annexin V-AbFluor™ 488/PI Apoptosis Detection kit (Abbkine, China) was used to determine cell apoptosis. After collecting and washing HepG2 and HUH7 cells with cold PBS three times, approximately 1.5×10^5 cells were resuspended in 500 μ L of $1 \times$ binding buffer and stained with 5 μ L Annexin V-AbFluor™ 488 and 2 μ L Propidium Iodide (PI) for 15 minutes in the dark. The apoptosis rate of each group was immediately measured by flow cytometry (BD Biosciences, USA).

Mitochondrial Membrane Potential Assay

To detect early apoptosis, a JC-1 fluorescence probe (Beyotime, Jiangsu, China) was employed to analyze mitochondrial membrane potential was employed to fluorescence microscopy (LX71, Olympus, Tokyo, Japan). Following a 24-hour treatment, JC-1 staining was applied to HepG2 and HUH7 cells at 37 °C for 20 minutes in the dark. The cells were then twice washed with JC-1 staining buffer before being detected. The mean fluorescence intensity was measured using ImageJ software (National Institutes of Health, Bethesda, MD, USA).

Transwell Analysis

Cell migration was evaluated using Transwell plates (Costar, USA) with hole diameters of 8.0 μ m. A total of 10×10^4 cells were grown in 100 μ L of serum-free media, while 800 μ L of medium containing 10% FBS was introduced to the lower chamber as a stimulating agent. Following 24 hours, the cells were immobilized using a 4% paraformaldehyde solution. Subsequently, they were stained with a 0.5% crystal violet solution for a duration of 30 minutes. After washing with distilled water, the cells were quantified by counting.

In vivo Antitumor Study

This study was approved by the Ethics Committee for Animal Experiments of Harbin Medical University. All animal experimental procedures (including the mice euthanasia procedure) were conducted according to the Association for Assessment and Accreditation of Laboratory Animal Care and the Institutional Animal Care and Use Committee guidelines.

Female Balb/c thymus-free mice were procured from Liaoning Life Changsheng Biotechnology Co., LTD. (Liaoning Province, China) for in vivo testing. They were housed in a pathogen-free environment with a 12-hour light/dark cycle and acclimated to the surroundings over three days. HepG2 cells (3×10^6 cells/only) were administered subcutaneously. When the tumor reached 180–200 mm³, the mice were separated at random into four groups of five animals each. Group 1 (PBS as control), group 2 (808 nm laser irradiation for 10 min), group 3 ($Cs_xWO_3@NBs$ injection), and group 4 ($Cs_xWO_3@NBs$ injection with 808 nm laser irradiation for 10 min). In vivo treatment was performed by intratumoral injection. Mice in group 1 received 100 μ L of PBS, while mice in groups 3 and 4 received 100 μ L of $Cs_xWO_3@NBs$ (0.5 mg/mL). The tumor was irradiated with a near-infrared 808 nm laser (2 W/cm²) for 10 min after injection of $Cs_xWO_3@NBs$. Tumor volume and body weight were measured daily after treatment, and volume was calculated using the formula volume = (tumor length) \times (tumor width)²/2. The weight and tumor size of each mouse were monitored during the study.

Histology Analysis

The tumor and main organs of mice (heart, liver, spleen, lung, and kidney) were cut, fixed with 4% paraformaldehyde, and embedded in paraffin. For histological investigation, the main organ and tumor sections were stained with H&E to determine the degree of necrosis in the tumor and the injury of related organs. TUNEL immunohistochemistry was used

simultaneously to stain the tumor slices by TUNEL cell apoptosis detection kit (Beyotime, Jiangsu, China). Images of apoptotic cells were examined and photographed using a microscope.

Statistical Analysis

Statistical analysis was performed using the GraphPad Prism 9.5.0 software (San Diego, CA, USA). The results were reported as the mean value plus or minus the standard deviation. The threshold for statistical significance was set at a *p*-value of less than 0.05. The statistical difference between the two groups was assessed using a Student's *t*-test, while a one-way analysis of variance was performed to compare several groups.

Results and Discussion

Synthesis and Characterization of Cs_xWO_3 and $Cs_xWO_3@NBs$

A water-controlled solvothermal synthesis procedure was used to create cesium-tungsten bronze Cs_xWO_3 , which has significant absorption in the near-infrared region and is useful for photothermal and photodynamic cancer treatment. In a nutshell, WCl_6 is fully dissolved in anhydrous ethanol initially, followed by the addition of $CsOH-H_2O$ and acetic acid after stirring. The resultant mixture is subsequently transferred to an electric oven for the solvent-thermal reaction, with a duration of 20 hours. During this procedure, the resulting deep blue material is cleansed and dehydrated. Ultimately, the Cs_xWO_3 is pulverized into a fine powder. Nanoparticles play a crucial role in anti-tumor therapy in the field of nanomedicine due to the Enhanced Permeability and Retention (EPR) effect, which allows them to carry therapeutic medicines. NBs were selected for this investigation based on their favorable characteristics of high biosafety and water solubility. In this experiment, we combined DSPC, DSPE, and biotin in certain proportions. Subsequently, we produced $Cs_xWO_3@NBs$ by using Cs_xWO_3 and C_3F_8 as the core, and a phospholipid membrane as the shell, through the processes of membrane hydration and shock.

The crystal phase of Cs_xWO_3 had been detected using X-ray diffraction. The results demonstrated that all of the sample's reflections match the hexagonal tungsten bronze of $Cs_{0.32}WO_3$ (PDF#83-1334) (Figure 1A). Their photophysical characteristics were investigated using ultraviolet-visible-near-infrared spectroscopy. The spectral study revealed that Cs_xWO_3 powder may greatly increase light absorption at 800–1200nm in the near-infrared region, with lower intensity and larger peak width (Figure 1B). Furthermore, in the near-infrared range, the absorbance increased with the increase of Cs_xWO_3 dispersion concentration, showing a good linear association (Figure 1C and D). $Cs_xWO_3@NBs$ also showed the typical absorbance peak of Cs_xWO_3 , showing that Cs_xWO_3 was integrated into the NBs (Figure 1E). The particle size determined by DLS was 477.3 ± 103.0 nm, which was comparable with the TEM data (Figure 1F). The TEM images of $Cs_xWO_3@NBs$ in PBS revealed that they looked like spherical nanoparticles due to the phospholipid microvesicle coating (Figure 1G). The average zeta potential for the NBs surface was -3.18 ± 0.47 mV (Figure 1H). To see if the $Cs_xWO_3@NBs$ change in various media, we also quantified the particle size and the zeta potential of the $Cs_xWO_3@NBs$ in the culture solution. According to Figure 1I, the particle size was 527.9 ± 75.44 nm, which was comparable with the TEM data (Figure 1J). Figure 1K showed that the zeta potential was -2.85 ± 0.23 mV. Since the size and the zeta potential of the $Cs_xWO_3@NBs$ in the culture solution were approximate to the in PBS, the medium has no appreciable impact on the size or potential of the $Cs_xWO_3@NBs$. To assess the stability of $Cs_xWO_3@NBs$, the material was subjected to ambient temperature conditions for a duration of 24 hours, during which electron microscope images were captured. As shown in Figure 1L, $Cs_xWO_3@NBs$ remained spherical, with an observed increase in particle size. The particle size determined by DLS was 803.4 ± 120.6 nm, and most particle size was in the nanometer range (Figure S1A). The average zeta potential was -2.33 ± 0.10 mV, indicating a decrease in stability at 24h (Figure S1B).

Photoabsorption and Photothermal Properties of Cs_xWO_3

To test the viability of Cs_xWO_3 as a photothermal absorber, we used a NIR laser (laser power 2 W/cm^2) as a light source and carefully observed the photothermal effect of Cs_xWO_3 distributed in PBS solution. As shown in Figure 2A, following laser irradiation, the sample quickly heated and stabilized after approximately 5 minutes. Furthermore, a significant dose-dependent temperature rise was detected, meaning that the greater the concentration, the faster the temperature increased. After 10 minutes of irradiation, the highest temperatures of 0.0625, 0.125, 0.25, 0.5, and 1.0 mg/

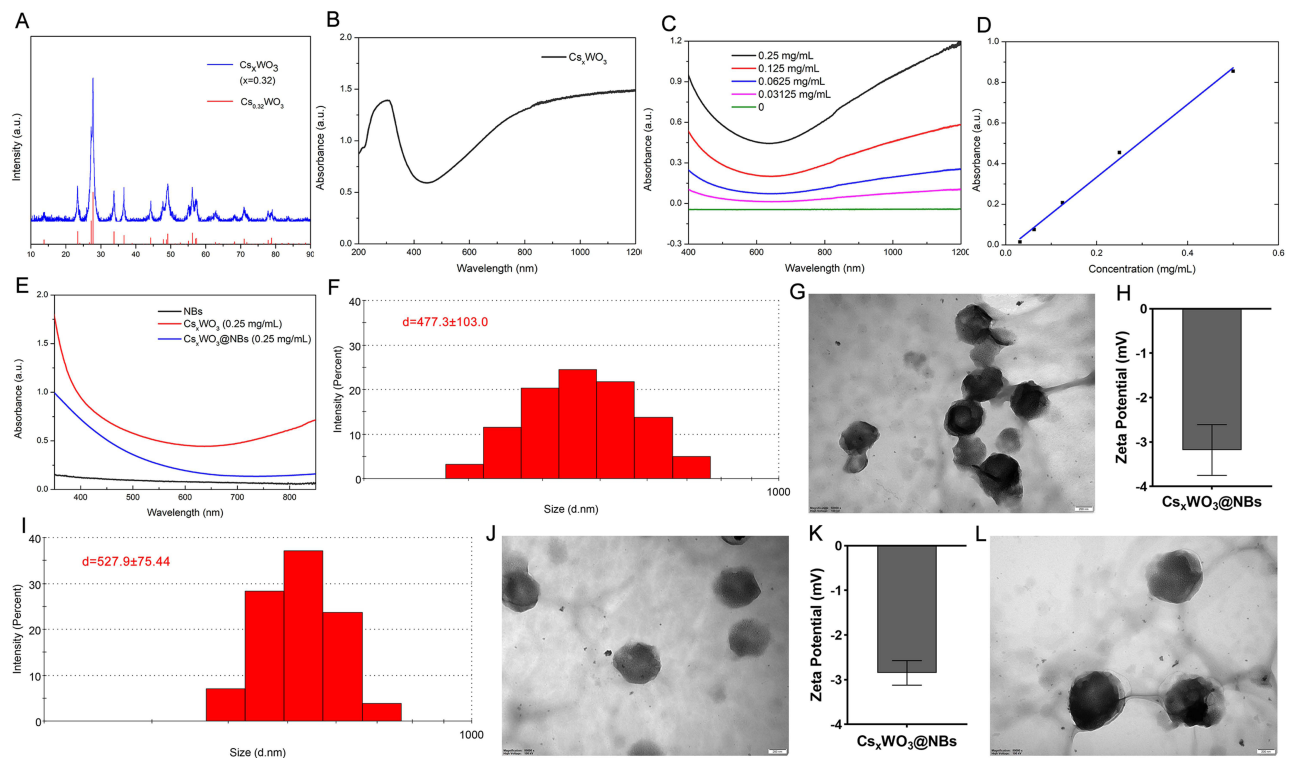


Figure 1 Characterization of the Cs_xWO_3 and $Cs_xWO_3@NBs$. (A) XRD pattern of Cs_xWO_3 . (B) UV-Vis-NIR absorption spectra of the Cs_xWO_3 powder. (C) UV-Vis-NIR absorption spectra of the Cs_xWO_3 dispersion with various concentrations. (D) The concentration absorption intensity curve of Cs_xWO_3 dispersion. (E) Absorption spectra of $Cs_xWO_3@NBs$, Cs_xWO_3 , and NBs. (F) Hydrodynamic diameter of $Cs_xWO_3@NBs$ in PBS at 0 h. (G) Transmission electron microscopy (TEM) image of $Cs_xWO_3@NBs$ in PBS at 0 h. (H) Zeta potential of $Cs_xWO_3@NBs$ in PBS at 0 h. (I) Hydrodynamic diameter of $Cs_xWO_3@NBs$ in the culture solution at 0 h. (J) Transmission electron microscopy (TEM) image of $Cs_xWO_3@NBs$ in the culture solution at 0 h. (K) Zeta potential of $Cs_xWO_3@NBs$ in the culture solution at 0 h. (L) TEM image of the $Cs_xWO_3@NBs$ in PBS stored at 37 °C for 24 h.

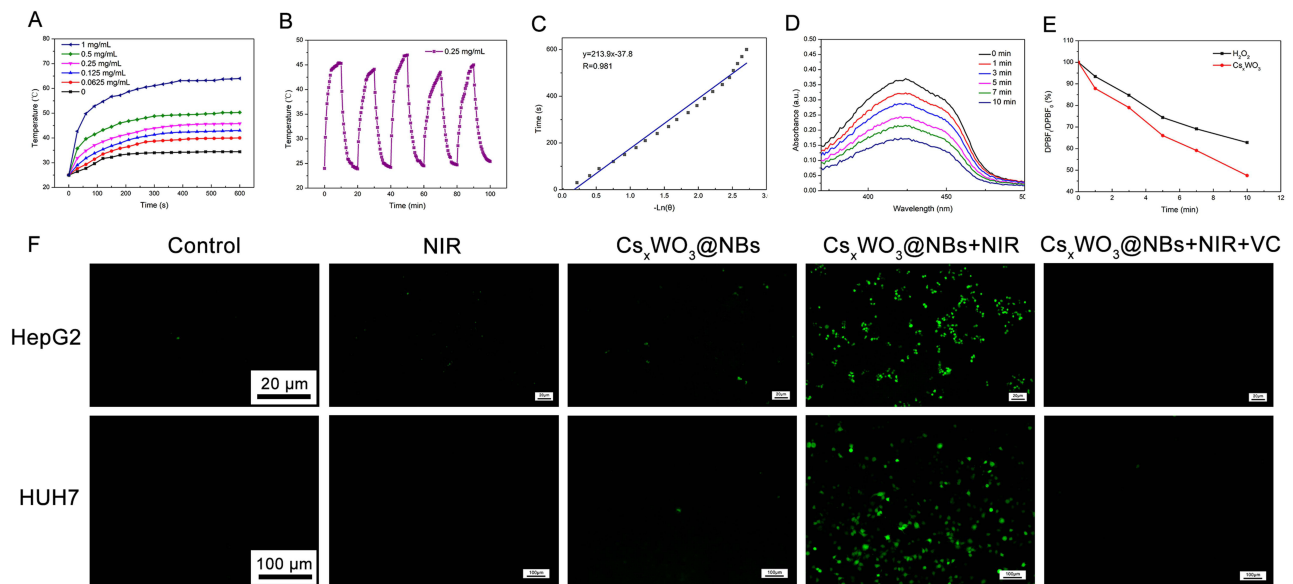


Figure 2 Photoabsorption and photothermal properties. (A) Temperature elevation curves of the Cs_xWO_3 dispersion with different concentrations under NIR laser irradiation (808 nm, 2 W/cm²). (B) Temperature curve of the Cs_xWO_3 (0.25 mg/mL) dispersion under NIR irradiation and in the absence of NIR irradiation. (C) The curve of $-\ln(I)$ versus time. (D) DPBF absorbance at different light times. (E) DPBF absorbance decline curve. (F) Detection of intracellular ROS generation.

mL Cs_xWO_3 dispersions reached 40, 43, 45.8, 50.3, and 64 °C, respectively. To further illustrate the photothermal characteristics of Cs_xWO_3 , we employed a sample concentration of 0.25 mg/mL for consecutive exposure to NIR laser. As shown in Figure 2B, Cs_xWO_3 exhibits exceptional photothermal stability. Upon the cessation of laser irradiation, the

temperature of the material will rapidly decrease within a brief timeframe. The photothermal conversion efficiency, determined by analyzing the temperature rise and fall curve and the curve depicting the temperature rise of pure water, is 42.7% (Figure 2C). These findings indicate that Cs_xWO_3 nanocrystals have the potential to function as a highly efficient photocatalytic material.

Detection of ROS Generation

Another emphasis of this research is the use of Cs_xWO_3 as a ROS-generating photosensitizer. Previously, analogs of cesium-tungsten bronze were utilized as NIR-driven photocatalysts to degrade organic dyes by producing ROS. Similarly, the Cs_xWO_3 employed in this investigation is predicted to exhibit photodynamic properties. In this part, we look at ROS formation via photoexcitation of Cs_xWO_3 in aqueous solution and in vitro tests. First, ROS formation in an aqueous solution was examined with a DPBF probe, which may react with ROS and diminish its distinctive absorbance at 410 nm. As a result, spectrophotometry-measured DPBF absorption loss may be used to indirectly estimate ROS levels. With the increase of irradiation time, the absorbance of DPBF gradually decreased (Figure 2D), indicating that Cs_xWO_3 continued to produce ROS. Figure 2E displayed the ratio of absorbance drop of DPBF at 410nm in aqueous and Cs_xWO_3 solutions following laser irradiation. Because the detecting environment cannot prevent light, and DPBF is extremely photosensitive, the absorbance of the DPBF-containing aqueous solution diminishes. However, as compared to an aqueous solution containing DPBF, the absorbance of the Cs_xWO_3 solution at 410nm was dramatically lowered under near-infrared irradiation, indicating that Cs_xWO_3 has a high ROS production potential.

Because the microenvironment within cancer cells differs significantly from that of water, it is critical to evaluate intracellular ROS levels to establish their potential as a photodynamic agent. In the intracellular ROS experiment, we added $Cs_xWO_3@NBs$. In addition, we investigated ROS formation in HepG2 cells using a non-fluorescent probe of DCFH-DA, which can be converted into green fluorescent 2', 7'-dichlorofluorescein (DCF) when ROS is present. As observed in Figure 2F, no cells in the control, NIR treatment, and $Cs_xWO_3@NBs$ treatment groups showed noticeable green fluorescence. In sharp contrast, HepG2 and HUH7 cells treated with $Cs_xWO_3@NBs$ and NIR irradiation displayed obvious green fluorescence. After adding ROS quencher VC, no green fluorescence was seen. All of the aforementioned outstanding ROS test findings indicate that $Cs_xWO_3@NBs$ might be employed as a PDT medicinal agent.

In vitro and in vivo US and CT Imaging

The phospholipid nanobubbles used to encapsulate Cs_xWO_3 and C_3F_8 are structurally comparable to traditional ultrasonic contrast agents in that they both employ phospholipid membranes to encapsulate the gas and create bubbles. As a result, we believe that $Cs_xWO_3@NBs$ might serve as a novel ultrasonic contrast agent. Therefore, $Cs_xWO_3@NBs$ in vitro bimodal imaging was done. As demonstrated in Figure 3A and B, $Cs_xWO_3@NBs$ showed clear signals in B-mode and CEUS modes compared to the control group. The HepG2 tumor-bearing mice model was then subjected to in vivo US imaging. Sonovue, a commercial ultrasound contrast agent, was also employed for comparison study to show the usefulness of the contrast function of $Cs_xWO_3@NBs$ that we produced. The ultrasound probe was positioned on the mice tumor for scanning following the injection of sonovue and $Cs_xWO_3@NBs$ solution (0.5 mg/mL 100 μ L). According to the results, the $Cs_xWO_3@NBs$ solution increased the grey value in B-mode and created an excellent CEUS function, even if its CEUS function was somewhat poorer than sonovue's when compared to the control group (Figure 3C). $Cs_xWO_3@NBs$ could greatly enhance the grey value, according to ImageJ software's examination of the image (Figure 3D). The findings validated the potential of $Cs_xWO_3@NBs$ as an ultrasound contrast agent.

Finally, the high ordinal number of W atoms enables $Cs_xWO_3@NBs$ to be exploited as a possible CT imaging agent. Figures 3E depicted a functional connection between the Hounsfield unit (HU) value and the concentration of $Cs_xWO_3@NBs$ solution, with the signal increasing linearly with the concentration of the solution. To perform in vivo CT imaging, HepG2 tumor-bearing mice were injected with 100 μ L of $Cs_xWO_3@NBs$ solution (2.5 mg/mL 100 μ L). As shown in Figure 3F, compared to the control group, the tumor of mice injected with $Cs_xWO_3@NBs$ showed a clear CT scanning effect, suggesting that $Cs_xWO_3@NBs$ had promise as a CT imaging agent. The findings above demonstrated that $Cs_xWO_3@NBs$ had good CEUS and CT imaging functions. $Cs_xWO_3@NBs$ exhibited promising potential to become

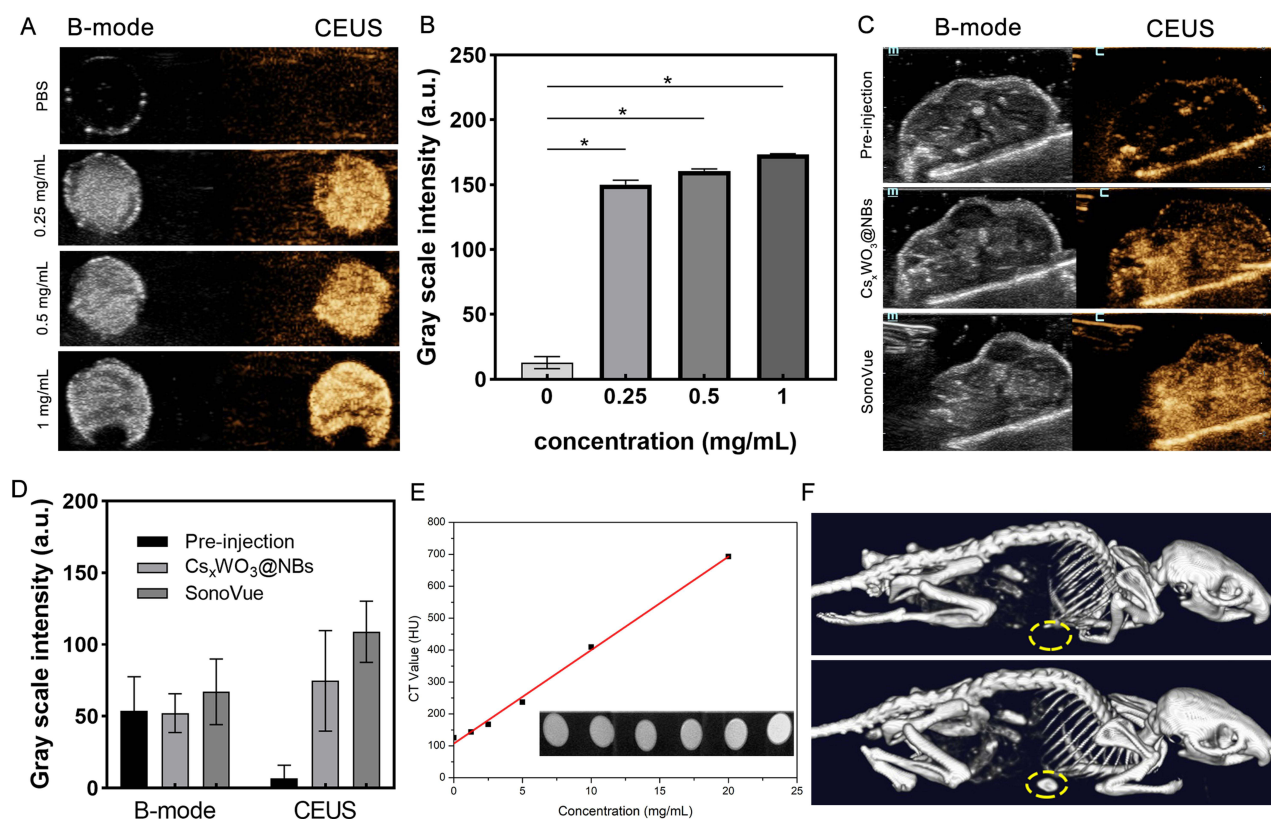


Figure 3 Ultrasound and CT images of Cs_xWO₃@NBs. (A) In vitro B-mode and CEUS images of the Cs_xWO₃@NBs dispersion with different concentrations. (B) The corresponding grayscale intensity of CEUS imaging in vitro. (C) B-mode and CEUS images of the HepG2-tumor-bearing mice before and after the intratumoral injection of Cs_xWO₃@NBs or SonoVue. (D) The corresponding grayscale intensity of B-mode and CEUS imaging in vivo. (E) In vitro CT phantom images and HU of the Cs_xWO₃@NBs dispersion with different concentrations. (F) In vivo CT images of HepG2-tumor-bearing mice before and after the intratumoral injection of Cs_xWO₃@NBs. *p<0.01, n=3.

a novel multifunctional contrast agent, capable of facilitating precise positioning and guiding therapeutic efficacy in medical treatments.

In vitro Phototherapeutic Investigation

The conventional CCK method was used to assess the cytotoxicity of Cs_xWO₃@NBs. After being exposed to Cs_xWO₃@NBs aqueous dispersion for 24 hours, HepG2 and HUH7 cells were detected using a kit. As seen in Figure 4A, Cs_xWO₃@NBs exhibited adequate biocompatibility and minimal toxicity in the concentration range below 0.25 mg/mL. In Figure 4A, Cs_xWO₃@NBs had a dose-dependent inhibitory effect on HepG2 and HUH7 cells when exposed to NIR radiation. Based on the results of the maximal half inhibition concentration (IC₅₀), the Cs_xWO₃@NBs concentration of HepG2 and HUH7 cells treated in future in vitro tests was established at 0.125 mg/mL and 0.25 mg/mL, respectively. We attempted to differentiate between the roles of PDT and PTT in the tests that followed. HepG2 and HUH7 cells were exposed to NIR (2.0 W/cm²) for 10 min after being treated with Cs_xWO₃@NBs (0.125 mg/mL, 0.25 mg/mL) for 2 hours. Due to the simultaneous production of ROS and hyperthermia, this group could demonstrate the synergistic effect of PTT/PDT (abbreviated PTT/PDT). The aforementioned, well-proven ROS quencher, VC, was then introduced during extracorporeal phototherapy to completely abolish the PDT effect. Consequently, the single factor contributing to this group of cell death (referred to as PTT) is heat. Another experimental group used an ice bath for the extracorporeal phototherapy procedure, keeping the irradiated cells at or below 20 °C. Only in this experiment can the PDT efficiency (denoted as PDT) be guaranteed. As Figure 4B illustrated, PDT and PTT treatments both caused some degree of cancer cell death as compared to the control group. Nevertheless, the application of both therapies resulted in a decrease in the survival rate of tumor cells to 53.6%±1.6% and 41.9%±0.5%, demonstrating that the combined PTT/PDT treatment had a substantial and noteworthy impact on the killing of tumor cells. Next, HepG2 and HUH7 cells were treated separately

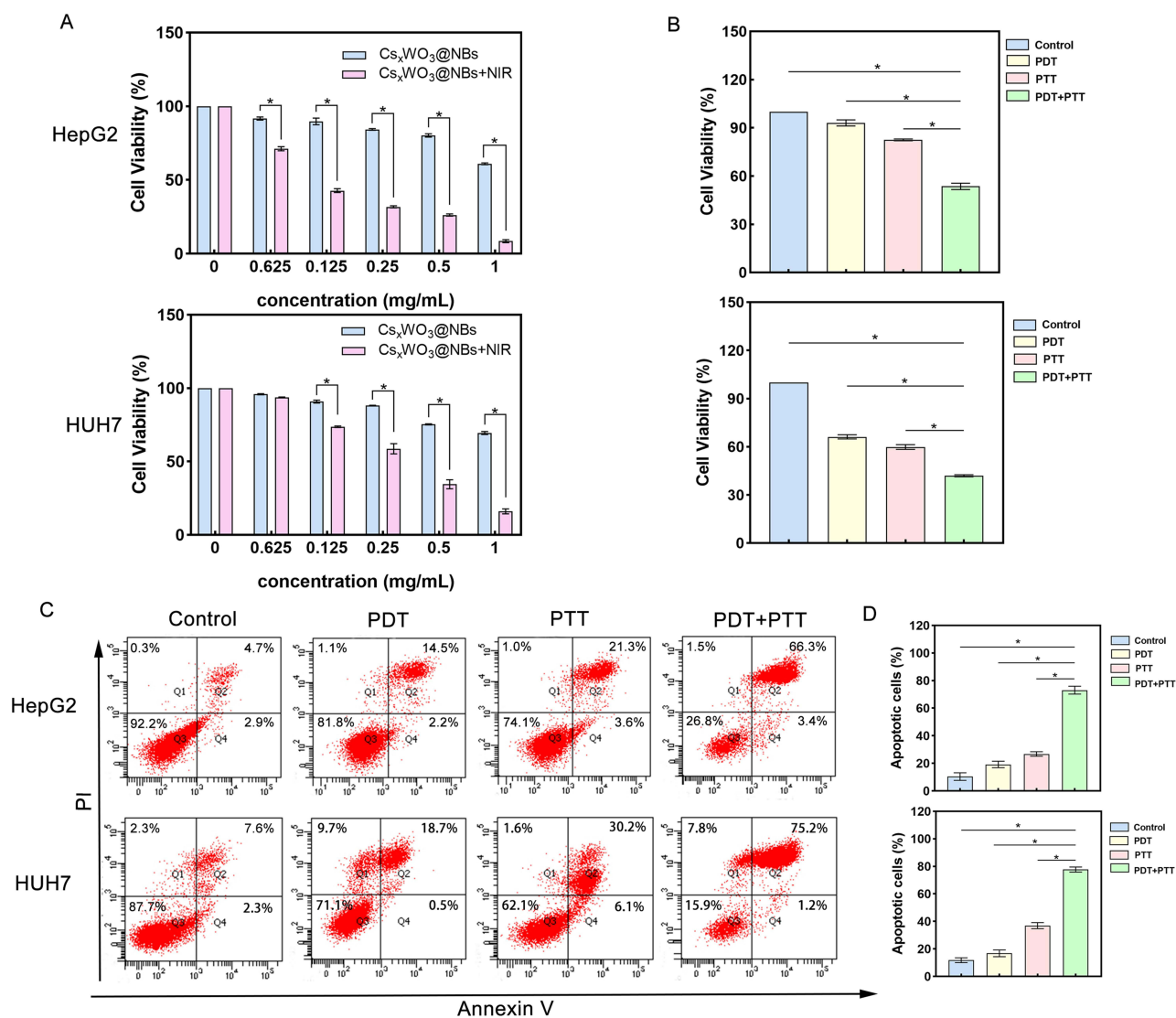


Figure 4 Cytotoxic effect of $Cs_xWO_3@NBs$ in HepG2 and HUH7 cells. **(A)** HepG2 and HUH7 cells were treated with $Cs_xWO_3@NBs$ (concentration: 0.0625–1 mg/mL) for 24 h, and the cell survival rate was detected by the CCK-8 assay. **(B)** HepG2 and HUH7 cells were treated with different treatments, and the cell survival rate was detected by the CCK-8 assay. **(C)** HepG2 and HUH7 cells were treated with different treatments for 24 h and then stained with Annexin-V and PI before being analyzed by flow cytometry **(D)** Statistical results from different experiments of cell apoptosis in HepG2 and HUH7 cells. * $p < 0.01$.

for 24 hours according to the above groups, and apoptosis was measured. Flow cytometry was used to identify apoptosis following double labeling with PI and Annexin V. As shown in Figure 4C, $Cs_xWO_3@NBs+NIR$ mediated photothermal and photodynamic combined therapy can induce apoptosis of cells. Figure 4D showed that HepG2 and HUH7 cells in the combination treatment group had significantly higher apoptosis rates ($73.1 \pm 2\%$ and $77.7 \pm 1.3\%$, respectively) compared to other treatment groups ($p < 0.01$). Flow cytometry findings were consistent with the results of CCK detection, indicating that the combination treatment effectively increased the apoptosis of HepG2 and HUH7 cells generated by phototherapy. Following, we hypothesize that phototherapy-induced cancer cell death is linked to the disturbance of mitochondrial membrane potential (MMP). The reduction in mitochondrial membrane potential is one of the early indicators of apoptosis. To investigate the alterations in MMP, we utilized JC-1 fluorescent dye. At greater MMP, JC-1 appears in the form of a polymer (J-aggregates), which emits red fluorescence. When MMP is lowered, JC-1 appears as a monomer and can emit green fluorescence. As a result, the change in JC-1 fluorescence from red to green can be utilized to detect early apoptosis. Figure 5A and B illustrated that a decrease in the fluorescence intensity ratio between the JC-1 aggregate (red) and the monomer (green) indicated a decrease in mitochondrial membrane potential.

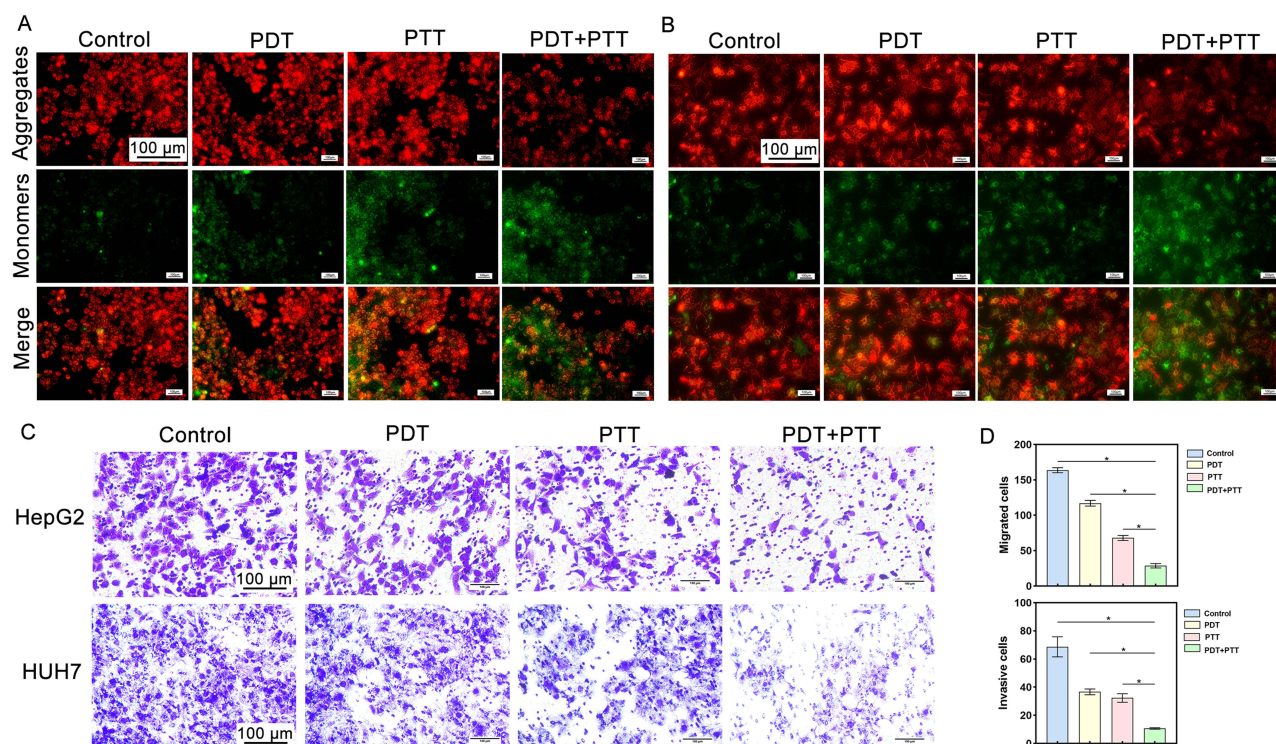


Figure 5 Detection of intracellular MMP changes and migration ability changes after different treatments. **(A)** Fluorescence microscopic imaging of HepG2 and **(B)** HUH7 cells stained by JC-1. **(C)** Representative images of HepG2 cells and HUH7 with migration ability after different treatments. **(D)** Quantitative analysis of cells with migration capacity at the bottom of the upper chamber. * $p < 0.01$.

Phototherapy might potentially induce apoptosis by utilizing a mitochondria-dependent mechanism. Another statistic used to assess the effectiveness of tumor therapy is the change in tumor cell migration capabilities. The transwell technique was used to analyze the migratory capability of HepG2 and HUH7 cells. Photographs were captured following crystal violet staining, and the visual results demonstrated a significant decrease in the number of migrating cells in the group that had combined PDT and PTT therapy, as compared to the other three groups (Figure 5C). Quantitative analysis of the number of cells traversed by ImageJ showed that the combination of PDT and PTT had a significant inhibitory effect on the migration of cancer cells (Figure 5D). Hence, the combined therapy could effectively inhibit the migration of HepG2 and HUH7 cells.

In vivo Phototherapeutic Investigation

The efficacy of extracorporeal phototherapy, mentioned above, motivated us to do additional in vivo investigations in mice. The model animals used were nude mice with HepG2 tumors. Before treatment, mice with 180–200 mm³ tumors were randomly separated into four groups ($n=5$ in each group) and given different therapies. Group 1 was the blank control group, group 2 was irradiated with a NIR 808 nm laser for 10 minutes, group 3 was injected with Cs_xWO₃@NBs, and group 4 was treated combining Cs_xWO₃@NBs and a NIR 808 nm laser. Following intratumoral injection, the medication covers the tumor after progressively spreading throughout it. Fluorescence imaging, which displays the drug's diffusion rate after injection, was used to determine the best timing for phototherapy intervention. As shown in Figure S2A, the DIR-Cs_xWO₃@NBs essentially covered the tumor in about two hours after injection, and the drug diffusion area grew over time. The tumor location fluorescence intensity curve is displayed in Figure S2B. In light of the findings of fluorescence imaging tests, we decided to begin NIR irradiation two hours after injection. The results of in vivo grouping treatment are as follows. As shown in Figure 6A, there was no significant difference in body weight among the four groups, indicating that the synergistic phototherapy of Cs_xWO₃@NBs produced under NIR induction had no acute toxicity. Through an analysis of the data on changes in tumor volume and tumor anatomical outcomes after

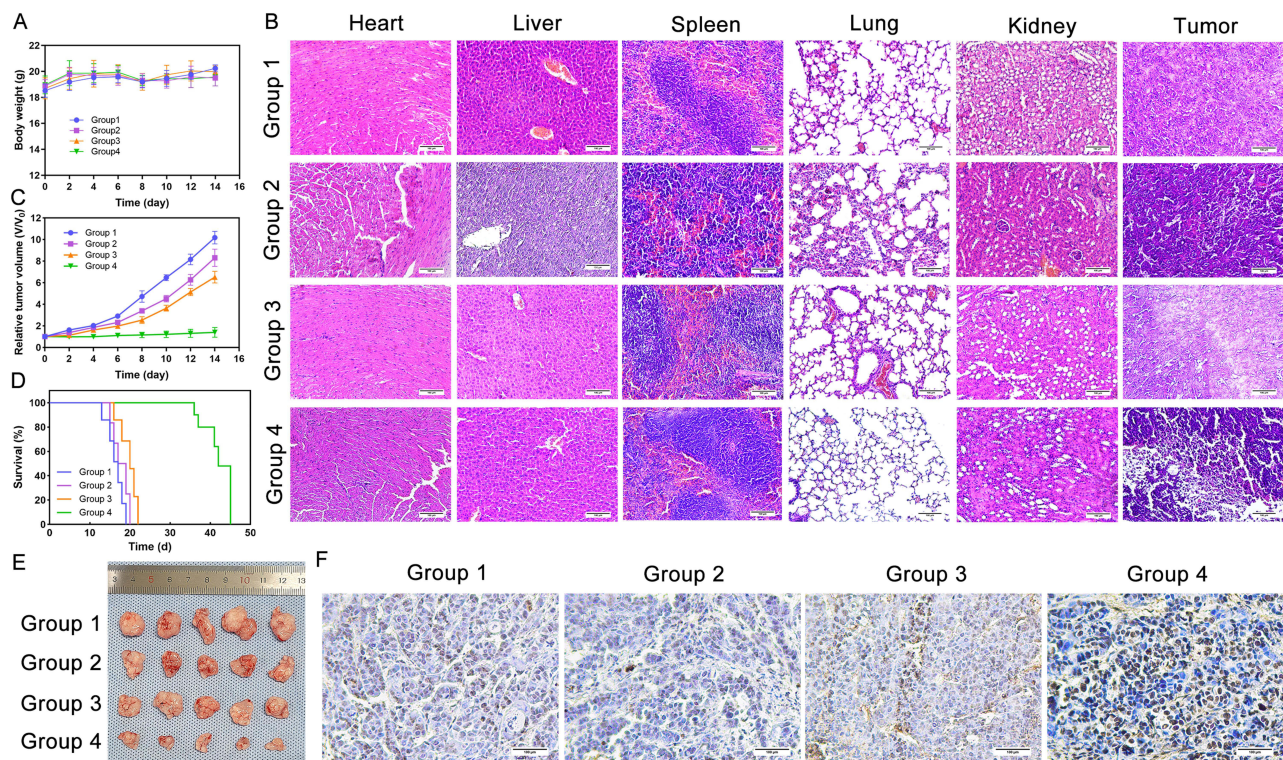


Figure 6 $Cs_xWO_3@NBs+NIR$ inhibits the growth of HepG2-tumor in vivo. (A) The curve of body weight of mice over time. (B) H&E staining of major organ slides and tumors of the mice. (C) The curve of relative tumor volume over time. (D) Survival curve of mice. (E) The anatomical photograph of the tumors. (F) TUNEL staining of tumors of the mice.

treatment, we saw that the control group exhibited continuous growth, the single therapy group did not show any meaningful inhibitory effect on the tumor, but the combined treatment group 4 effectively suppressed tumor development (Figure 6C and E). We continually tracked the survival of four groups of ten mice each for a total observation time of forty-five days (measured from the commencement of treatment) in order to evaluate the impact of combination therapy on the survival of HepG2 tumor mice. Treated animal was euthanized when the tumor size reached the ethical end point. Mice in groups 1, 2, and 3 started to die on day 13, as seen in Figure 6D, and only group 4 mice were still alive on day 22. The combined therapy greatly increased the longevity of tumor-bearing mice, as demonstrated by the survival results of the fourth group of animals.

Solid tumor tissue was stained with H&E. Figure 6B showed that H&E staining was done on mice's primary organs (heart, liver, spleen, lung, and kidney) and tumors in four groups. The findings indicated that there were no evident histological abnormalities or lesions in any organ, showing that $Cs_xWO_3@NBs$ was organ-safe in vivo. H&E staining of tumors revealed a substantial quantity of necrosis in the combination group, but only a tiny amount of flaky necrosis in the other three groups. TUNEL staining was also carried out on HepG2 tumor sections. Apoptotic cells have genomic DNA breaks in their nuclei. Terminal Deoxynucleotidyl Transferase (TdT) can catalyze the exposed 3' OH of fragmented genomic DNA by adding biotin-labeled dUTP (Biotin-dUTP). Subsequently, Streptavidin tagged with horseradish peroxidase (HRP) was added to the mixture, and the apoptotic cells were ultimately visualized using DAB color development catalyzed by HRP. After staining the tumor tissue slice with the TUNEL chromogenic kit, the nucleus of apoptotic cells will appear brown. The nuclei were first stained with hematoxylin dye and then treated the sections with TUNEL staining. Figure 6F showed that the combined treatment group had the most brown-stained nuclei, whereas the other three groups had only a few. These findings suggested that the combination of PDT and PTT treatment can promote tumor cell death. The findings of H&E and TUNEL staining on tumor tissue sections revealed that the combination treatment significantly inhibited tumor development.

Conclusions

This study created a new type of tungsten bronze Cs_xWO_3 by inserting cesium ions into the orthorhombic WO_3 skeleton. Empirical investigations and theoretical simulations have verified the exceptional and extensive NIR absorption characteristics of Cs_xWO_3 . This substance possesses the capacity to produce elevated temperatures and reactive oxygen species (ROS), leading to a combined therapeutic impact of PTT and PDT. Therefore, due to the benefits of Cs_xWO_3 -mediated synergistic phototherapy, we effectively produced antitumor effects. It is noteworthy that Cs_xWO_3 coated with the phospholipid nanovesicles demonstrates optimum biocompatibility, typically minimal cytotoxicity. $Cs_xWO_3@NBs$ have a high order number of W elements and gas-containing nanobubbles, making them suitable for CT and ultrasound imaging and tumor visualization in vivo. Our findings show that $Cs_xWO_3@NBs$, as a photosensitizer and bimodal imaging agent, will give fresh ideas for the future development of non-invasive tumor therapy, as well as new possibilities for cancer treatment in the clinic.

Acknowledgments

The experimental site was provided by Cancer Research affiliated with Harbin Medical University.

Funding

This research was supported by the Key Project of Heilongjiang Provincial Natural Science Foundation of China (grant number ZD2021H005), and the National Natural Science Foundation of China (grant number 82171947).

Disclosure

The authors report no conflicts of interest in this work.

References

1. Wang X, Wang C, Tian H, Chen Y, Wu B, Cheng W. IR-820@NBs combined with MG-132 enhances the anti-hepatocellular carcinoma effect of sonodynamic therapy. *Int J Nanomed.* 2023;18:6199–6212. doi:10.2147/ijn.S431910
2. Chen Y, Shang H, Wang C, et al. RNA-Seq explores the mechanism of oxygen-boosted sonodynamic therapy based on all-in-one nanobubbles to enhance ferroptosis for the treatment of HCC. *Int J Nanomed.* 2022;17:105–123. doi:10.2147/IJN.S343361
3. Lin J, Rao D, Zhang M, Gao Q. Metabolic reprogramming in the tumor microenvironment of liver cancer. *J Hematol Oncol.* 2024;17(1). doi:10.1186/s13045-024-01527-8
4. Zhou J, Sun H, Wang Z, et al. Guidelines for the diagnosis and treatment of primary liver cancer (2022 Edition). *Liver Cancer.* 2023;12(5):405–444. doi:10.1159/000530495
5. Miller KD, Nogueira L, Devasia T, et al. Cancer treatment and survivorship statistics, 2022. *CA Cancer J Clin.* 2022;72(5):409–436. doi:10.3322/caac.21731
6. Mai B, Wang X, Liu Q, Zhang K, Wang P. The application of DVDMS as a sensitizing agent for sono-/photo-therapy. *Front Pharmacol.* 2020;11:19. doi:10.3389/fphar.2020.00019
7. Cai J, Yang Y, Zhang J, et al. Multilayer nanodrug delivery system with spatiotemporal drug release improves tumor microenvironment for synergistic anticancer therapy. *Biofabrication.* 2024;16(2):025012. doi:10.1088/1758-5090/ad22ef
8. Bian H, Ma D, Zhang X, et al. Tailored engineering of novel xanthonium polymethine dyes for synergistic PDT and PTT triggered by 1064 nm laser toward deep-seated tumors. *Small.* 2021;17(21). doi:10.1002/smll.202100398
9. Campu A, Focsan M, Lerouge F, et al. ICG-loaded gold nano-bipyramids with NIR activatable dual PTT-PDT therapeutic potential in melanoma cells. *Colloids Surf B.* 2020;194:111213. doi:10.1016/j.colsurfb.2020.111213
10. Guo X, Li L, Jia W, et al. Composite nanomaterials of conjugated polymers and upconversion nanoparticles for NIR-triggered photodynamic/photothermal synergistic cancer therapy. *ACS Appl Mater Interfaces.* 2023. doi:10.1021/acsami.3c12553
11. Jin T, Cheng D, Jiang G, et al. Engineering naphthalimide-cyanine integrated near-infrared dye into ROS-responsive nanohybrids for tumor PDT/PTT/chemotherapy. *Bioact Mater.* 2022;14:42–51. doi:10.1016/j.bioactmat.2021.12.009
12. Wang H, Su D, Huang R, Shu F, Cheng F, Zheng G. Cellular nanovesicles with bioorthogonal targeting enhance photodynamic/photothermal therapy in psoriasis. *Acta Biomater.* 2021;134:674–685. doi:10.1016/j.actbio.2021.07.068
13. Shao W, Yang C, Li F, et al. Molecular design of conjugated small molecule nanoparticles for synergistically enhanced PTT/PDT. *Nano-Micro Lett.* 2020;12(1). doi:10.1007/s40820-020-00474-6
14. Zhang D, Wu M, Zeng Y, et al. Chlorin e6 conjugated Poly(dopamine) nanospheres as PDT/PTT dual-modal therapeutic agents for enhanced cancer therapy. *ACS Appl Mater Interfaces.* 2015;7(15):8176–8187. doi:10.1021/acsami.5b01027
15. Wang D, Zhang Z, Lin L, et al. Porphyrin-based covalent organic framework nanoparticles for photoacoustic imaging-guided photodynamic and photothermal combination cancer therapy. *Biomaterials.* 2019;223:119459. doi:10.1016/j.biomaterials.2019.119459
16. Dai T, He W, Tu S, et al. Black TiO₂ nanoprobe-mediated mild phototherapy reduces intracellular lipid levels in atherosclerotic foam cells via cholesterol regulation pathways instead of apoptosis. *Bioact Mater.* 2022;17:18–28. doi:10.1016/j.bioactmat.2022.01.013

17. Luo H, Gao S. Recent advances in fluorescence imaging-guided photothermal therapy and photodynamic therapy for cancer: from near-infrared-I to near-infrared-II. *J Control Release*. 2023;362:425–445. doi:10.1016/j.jconrel.2023.08.056
18. Zhang L, Liu Y, Huang H, et al. Multifunctional nanotheranostics for near infrared optical imaging-guided treatment of brain tumors. *Adv Drug Deliv Rev*. 2022;190. doi:10.1016/j.addr.2022.114536
19. Kim HS, Seo M, Park T-E, Lee DY. A novel therapeutic strategy of multimodal nanoconjugates for state-of-the-art brain tumor phototherapy. *J Nanobiotechnol*. 2022;20(1). doi:10.1186/s12951-021-01220-9
20. Felsher DW. Cancer revoked: oncogenes as therapeutic targets. *Nat Rev Cancer*. 2003;3(5):375–380. doi:10.1038/nrc1070
21. Castano AP, Demidova TN, Hamblin MR. Mechanisms in photodynamic therapy: part one—photosensitizers, photochemistry and cellular localization. *Photodiagn Photodyn Ther*. 2004;1(4):279–293. doi:10.1016/s1572-1000(05)00007-4
22. Cheng L, Wang C, Feng L, Yang K, Liu Z. Functional nanomaterials for phototherapies of cancer. *Chem Rev*. 2014;114(21):10869–10939. doi:10.1021/cr400532z
23. Agostinis P, Berg K, Cengel KA, et al. Photodynamic therapy of cancer: an update. *CA Cancer J Clin*. 2011;61(4):250–281. doi:10.3322/caac.20114
24. Li X-Y, Li Y-M, Kong R-J, et al. Feedback-elevated antitumor amplifier of self-delivery nanomedicine by suppressing photodynamic therapy-caused inflammation. *ACS Appl Bio Mater*. 2023;6(7):2816–2825. doi:10.1021/acsabm.3c00263
25. Zheng Q, Liu X, Zheng Y, et al. The recent progress on metal-organic frameworks for phototherapy. *Chem Soc Rev*. 2021;50(8):5086–5125. doi:10.1039/d1cs00056j
26. Chen H, Wu L, Wang T, et al. PTT/PDT-induced microbial apoptosis and wound healing depend on immune activation and macrophage phenotype transformation. *Acta Biomater*. 2023;167:489–505. doi:10.1016/j.actbio.2023.06.025
27. Liu T, Chen Y, Wang H, et al. Phototheranostic agents based on nonionic heptamethine cyanine for realizing synergistic cancer phototherapy. *Adv Healthcare Mater*. 2023;12(11). doi:10.1002/adhm.202202817
28. Dai X, Liu D, Pan P, Liang G, Wang X, Chen W. Multifunctional two-dimensional Bi₂Se₃ nanodisks as a non-inflammatory photothermal agent for glioma treatment. *J Colloid Interface Sci*. 2024;661:930–942. doi:10.1016/j.jcis.2024.01.130
29. Overchuk M, Weersink RA, Wilson BC, Zheng G. Photodynamic and photothermal therapies synergy opportunities for nanomedicine. *ACS Nano*. 2023;17(9):7979–8003. doi:10.1021/acsnano.3c00891
30. Liu K, Zhang L, Lu H, et al. Enhanced mild-temperature photothermal therapy by pyroptosis-boosted ATP deprivation with biodegradable nanoformulation. *J Nanobiotechnol*. 2023;21(1). doi:10.1186/s12951-023-01818-1
31. Chang M, Hou Z, Wang M, Li C, Lin J. Recent advances in hyperthermia therapy-based synergistic immunotherapy. *Adv Mater*. 2021;33(4):e2004788. doi:10.1002/adma.202004788
32. Zhou Z, Yan Y, Hu K, et al. Autophagy inhibition enabled efficient photothermal therapy at a mild temperature. *Biomaterials*. 2017;141:116–124. doi:10.1016/j.biomaterials.2017.06.030
33. Tao Q, He G, Ye S, et al. Mn doped Prussian blue nanoparticles for T1/T2 MR imaging, PA imaging and Fenton reaction enhanced mild temperature photothermal therapy of tumor. *J Nanobiotechnol*. 2022;20(1). doi:10.1186/s12951-021-01235-2
34. Song X, Wang M, Liu S, et al. A sequential scheme including PTT and 2'3'-cGAMP/CQ-LP reveals the antitumor immune function of PTT through the type I interferon pathway. *Pharmacol Res*. 2023;196doi:10.1016/j.phrs.2023.106939.
35. Wu Q, Niu M, Chen X, et al. Biocompatible and biodegradable zeolitic imidazolate framework/polydopamine nanocarriers for dual stimulus triggered tumor thermo-chemotherapy. *Biomaterials*. 2018;162:132–143. doi:10.1016/j.biomaterials.2018.02.022
36. Jayasankar G, Koilpillai J, Narayanasamy D. A systematic study on long-acting nanobubbles: current advancement and prospects on theranostic properties. *Adv Pharm Bull*. 2024;14(2):278–301. doi:10.34172/apb.2024.042
37. Tian J, Yang F, Cui H, Zhou Y, Ruan X, Gu N. A novel approach to making the gas-filled liposome real: based on the interaction of lipid with free nanobubble within the solution. *ACS Appl Mater Interfaces*. 2015;7(48):26579–26584. doi:10.1021/acsami.5b07778
38. Johansen ML, Perera R, Abenojar E, et al. Ultrasound-based molecular imaging of tumors with PTPmu biomarker-targeted nanobubble contrast agents. *Int J Mol Sci*. 2021;22(4):1983. doi:10.3390/ijms22041983
39. Astafyeva K, Somaglino L, Desgranges S, et al. Perfluorocarbon nanodroplets stabilized by fluorinated surfactants: characterization and potentiality as theranostic agents. *J Mater Chem B*. 2015;3(14):2892–2907. doi:10.1039/c4tb01578a
40. Lu X, Dou C, Fabiilli ML, Miller DL. Capillary hemorrhage induced by contrast-enhanced diagnostic ultrasound in rat intestine. *Ultrasound Med Biol*. 2019;45(8):2133–2139. doi:10.1016/j.ultrasmedbio.2019.04.012
41. Zhuge D, Li L, Wang H, et al. Bacterial toxin-responsive biomimetic nanobubbles for precision photodynamic therapy against bacterial infections. *Adv Healthcare Mater*. 2022;11(18). doi:10.1002/adhm.202200698
42. Hernandez C, Nieves L, de Leon AC, Advincula R, Exner AA. Role of surface tension in gas nanobubble stability under ultrasound. *ACS Appl Mater Interfaces*. 2018;10(12):9949–9956. doi:10.1021/acsami.7b19755
43. Duan L, Yang L, Jin J, et al. Micro/nano-bubble-assisted ultrasound to enhance the EPR effect and potential theranostic applications. *Theranostics*. 2020;10(2):462–483. doi:10.7150/thno.37593
44. Browning RJ, Able S, Ruan JL, et al. Combining sonodynamic therapy with chemoradiation for the treatment of pancreatic cancer. *J Control Release*. 2021;337:371–377. doi:10.1016/j.jconrel.2021.07.020
45. Sun Z, Gu Z, Ma W. Confined electrochemical behaviors of single platinum nanoparticles revealing ultrahigh density of gas molecules inside a nanobubble. *Anal Chem*. 2023;95(7):3613–3620. doi:10.1021/acs.analchem.2c04309
46. Abenojar EC, Bederman I, de Leon AC, et al. Theoretical and experimental gas volume quantification of micro- and nanobubble ultrasound contrast agents. *Pharmaceutics*. 2020;12(3):208. doi:10.3390/pharmaceutics12030208
47. Guo C, Yin S, Yu H, et al. Photothermal ablation cancer therapy using homogeneous CsxWO₃ nanorods with broad near-infrared absorption. *Nanoscale*. 2013;5(14):6469–6478. doi:10.1039/c3nr01025b
48. Li J, Liu D, Zhou D, Shao L, Chen X, Song H. Label-free photoelectrochemical biosensor for alpha-fetoprotein detection based on Au/CsxWO₃ heterogeneous films. *Talanta*. 2021;225:122074. doi:10.1016/j.talanta.2020.122074
49. Wen M, Wang S, Jiang R, et al. Tuning the NIR photoabsorption of CuWO_{4-x} nanodots with oxygen vacancies for CT imaging guided photothermal therapy of tumors. *Biomater Sci*. 2019;7(11):4651–4660. doi:10.1039/c9bm00995g

50. Qiu J, Xiao Q, Zheng X, et al. Single W18O49 nanowires: a multifunctional nanoplatform for computed tomography imaging and photothermal/photodynamic/radiation synergistic cancer therapy. *Nano Res.* 2015;8(11):3580–3590. doi:10.1007/s12274-015-0858-z
51. Gao Y, Wang F, Huang W, et al. Sn(x)WO(3) as a theranostic platform for realizing multi-imaging-guided photothermal/photodynamic combination therapy. *Nanoscale.* 2019;11(7):3300–3310. doi:10.1039/c8nr08771g

International Journal of Nanomedicine

Dovepress

Publish your work in this journal

The International Journal of Nanomedicine is an international, peer-reviewed journal focusing on the application of nanotechnology in diagnostics, therapeutics, and drug delivery systems throughout the biomedical field. This journal is indexed on PubMed Central, MedLine, CAS, SciSearch[®], Current Contents[®]/Clinical Medicine, Journal Citation Reports/Science Edition, EMBase, Scopus and the Elsevier Bibliographic databases. The manuscript management system is completely online and includes a very quick and fair peer-review system, which is all easy to use. Visit <http://www.dovepress.com/testimonials.php> to read real quotes from published authors.

Submit your manuscript here: <https://www.dovepress.com/international-journal-of-nanomedicine-journal>